Structure, thermodynamic properties, and phase diagrams of few colloids confined in a spherical pore

Iván E. Paganini, Claudio Pastorino, and Ignacio Urrutia

Citation: The Journal of Chemical Physics **142**, 244707 (2015); doi: 10.1063/1.4923164
View online: http://dx.doi.org/10.1063/1.4923164
View Table of Contents: http://scitation.aip.org/content/aip/journal/jcp/142/24?ver=pdfcov
Published by the AIP Publishing

Articles you may be interested in

Liquid-vapor phase diagram and surface properties in oppositely charged colloids represented by a mixture of attractive and repulsive Yukawa potentials
J. Chem. Phys. **138**, 054507 (2013); 10.1063/1.4789915

Phase behavior of repulsive polymer-tethered colloids
J. Chem. Phys. **132**, 014901 (2010); 10.1063/1.3273415

Many body effects on the phase separation and structure of dense polymer-particle melts
J. Chem. Phys. **128**, 234901 (2008); 10.1063/1.2938379

Phase behavior of a suspension of colloidal hard rods and nonadsorbing polymer
J. Chem. Phys. **124**, 234902 (2006); 10.1063/1.2202853

Effects of colloid polydispersity on the phase behavior of colloid-polymer mixtures
J. Chem. Phys. **122**, 074904 (2005); 10.1063/1.1851978

This article is copyrighted as indicated in the article. Reuse of AIP content is subject to the terms at: http://scitation.aip.org/termsconditions. Downloaded to IP: 168.96.66.153 On: Tue, 30 Jun 2015 17:10:17

Structure, thermodynamic properties, and phase diagrams of few colloids confined in a spherical pore

Iván E. Paganini,[1,2] Claudio Pastorino,[1,2,a)] and Ignacio Urrutia[1,2,b)]
[1]*Departamento de Física de la Materia Condensada, Centro Atómico Constituyentes, CNEA, Av.Gral. Paz 1499, 1650 Pcia. de Buenos Aires, Argentina*
[2]*CONICET, Avenida Rivadavia 1917, C1033AAJ Buenos Aires, Argentina*

(Received 9 April 2015; accepted 17 June 2015; published online 30 June 2015)

We study a system of few colloids confined in a small spherical cavity with event driven molecular dynamics simulations in the canonical ensemble. The colloidal particles interact through a short range square-well potential that takes into account the basic elements of attraction and excluded-volume repulsion of the interaction among colloids. We analyze the structural and thermodynamic properties of this few-body confined system in the framework of inhomogeneous fluids theory. Pair correlation function and density profile are used to determine the structure and the spatial characteristics of the system. Pressure on the walls, internal energy, and surface quantities such as surface tension and adsorption are also analyzed for a wide range of densities and temperatures. We have characterized systems from 2 to 6 confined particles, identifying distinctive qualitative behavior over the thermodynamic plane $T - \rho$, in a few-particle equivalent to phase diagrams of macroscopic systems. Applying the extended law of corresponding states, the square well interaction is mapped to the Asakura-Oosawa model for colloid-polymer mixtures. We link explicitly the temperature of the confined square-well fluid to the equivalent packing fraction of polymers in the Asakura-Oosawa model. Using this approach, we study the confined system of few colloids in a colloid-polymer mixture. © *2015 AIP Publishing LLC.* [http://dx.doi.org/10.1063/1.4923164]

I. INTRODUCTION

Over the last decades, colloid physics has been one of the areas of higher activity in the field of soft matter. In particular, dispersions of core/shell nanoparticles have been the subject of intense work in synthesis and characterization due to their promising applications for bioimaging, controlled drug release, and targeted drug delivery.[1,2] Core/shell nanoparticles also serve as templates for the preparation of hollow nanoparticles. The most widely synthesized geometry is the spherical hollow nanoparticle. However, newer approaches based on sol-gel techniques and colloidal templating can be employed to fabricate hollow nano-structures of a wide variety of sizes, shapes, and chemical properties, which expand even further the possible applications of hollow and yolk-shell[3] nanoparticles and nano-rattles.[4,5] The distribution of matter inside the particles plays an increasingly important role in determining the function of nanoparticles in applications such as catalysis, gene delivery, photonics, and nano-reactors.[1,4,6] The large fraction of empty space, for example, has been successfully used to encapsulate and control release-sensitive materials such as drugs, cosmetics, and DNA.[4] Therefore, understanding the structure and thermodynamic properties of few colloids in confinement is both interesting from the basic research point of view and potentially useful for these emerging applications.

On the other hand, polymer-colloid mixtures in spherical confinement have received strong attention recently in the context of miniemulsions, which are used as nanocontainers to produce polymer, ceramics, or metal nanoparticles.[7]

Some colloidal suspensions behave like hard spheres (HS), where the feature of the interacting potential is the repulsion length σ (particle diameter), related to the excluded volume.[8,9] Free energy and pressure of few HS colloids confined in a spherical pore have recently been studied with molecular dynamics and theoretical approaches.[10–13] In several cases, it is necessary to complement this hard-core repulsion with an attractive, short-range interaction to properly describe the potential between real colloidal particles. For this purpose, the square-well (SW) potential has been investigated extensively exploiting its simplicity.[14] Systems of SW colloids enable us to study colloids both in bulk and in confinement, not only through Monte Carlo and molecular dynamics simulations but also with analytic approaches. SW system is the simplest interaction model with tunable range, giving rise to phase transitions and coexistence regions. The thermodynamic properties, phases coexistence,[15–21] structure,[22] crystallization, glassy behavior,[23] and percolation phenomena[24] of short-range SW fluids were extensively studied in bulk. Properties of inhomogeneous SW systems at free interphases and in confinement were also studied.[24–28] Molecular dynamics studies to obtain bulk free energy of short range SW particles have been recently performed.[16,29] Pressure on the wall and structural properties were studied theoretically for two SW particles in a spherical cavity.[30] Liquid-vapor coexistence of SW fluid confined in cylindrical pores[31] and short range SW potential in the context of effective interactions among proteins[32] were also

a)pastor@cnea.gov.ar
b)iurrutia@cnea.gov.ar

 © 2015 AIP Publishing LLC

This article is copyrighted as indicated in the article. Reuse of AIP content is subject to the terms at: http://scitation.aip.org/termsconditions. Downloaded to IP: 168.96.66.153 On: Tue, 30 Jun 2015 17:10:17

studied. Colloid-polymer-mixtures in spherical confinement were analysed recently with the Asakura-Oosawa (AO) model.[33–35] Other works of the AO model with different values of diameter ratio have shown interesting properties in bulk, as glassy states and demixing.[36,37]

In this work, we study thoroughly highly confined colloids in spherical pores, that show different demeanor as compared to their bulk counterparts. The confining cavity (thought as a nanopore) breaks the translational symmetry of a system and causes the appearance of spatial variations. Even farther from bulk case, our aim is to work with low number of particles and a system size comparable to its constituent elements. This implies that we are far away from thermodynamic limit. Nevertheless, we work in the frame of statistical mechanics. In addition, low N systems allow for analytic solutions at some degree, thus letting us to make a direct comparison between theory and simulation results. On this line, we study the system of few short-range interacting colloids in a hard-wall spherical pore. The colloidal particles are studied by event-driven molecular dynamics simulations using the SW model in a wide range of number densities and relevant temperatures. We also map the simulated system to a colloid-polymer mixture in a spherical pore. In this case, we adopt the AO model and consider the case of small ratio of sizes between polymer and colloids σ_p/σ. We connect the short-range SW potential and the AO model by adopting the effective short-range colloid-colloid pair potential through an extended corresponding-states law, following that of Noro and Frenkel.[38,39]

The paper is organized as follows. In Sec. II, we provide details of the interaction model and the statistical mechanics theoretical grounds for both few body systems in pores: colloids modeled as short-range SW particles and colloid-polymer mixtures modeled as AO particles. In addition, we describe the extended law of corresponding states that is utilized to map between both few body systems. In Sec. III we present the simulation technique and the way we obtain canonical ensemble simulations at constant temperature for the SW system. Section IV is devoted to present the density profiles, pair correlation functions, thermodynamics properties, and phase diagrams of systems of 2–6 SW colloidal particles in a spherical cavity. In Fig. 1 we present two snapshots that show typical configurations of the studied systems at different temperatures. We analyze the results of the simulated colloidal suspension using the SW model, and also map these results for an equivalent colloid-polymer mixture of the AO model whenever possible. We present a final discussion and summary in Sec. V.

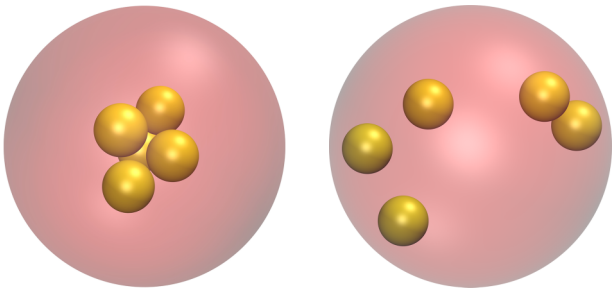

FIG. 1. Snapshots of the studied system. This case shows five particles (yellow) in a spherical pore (pink, transparent) at number density 0.1, and temperature $T = 0.1$ (left) and $T = 0.5$ (right). See text for more details.

II. THEORETICAL BACKGROUND

We study a system of N (ranging from 2 to 6) colloidal particles of diameter σ, confined in a spherical cavity of radius R_o at constant temperature T. The particles interact with the cavity through a hard wall potential that prevents them from escaping outside. Thus, the effective radius of the cavity is $R_{\text{eff}} \equiv R_o - \sigma/2$, which represents the maximum possible distance between the center of the cavity and the center of each colloid. The temperature of the fluid is determined by the wall temperature T, which is fixed. We adopt the effective volume $V = 4\pi R_{\text{eff}}/3$ to measure the size of the available space for particles and consistently define the mean number density $\rho = N/V$.

Given that we deal with a small number of colloids, the ensemble's equivalence does not apply. The statistical mechanical and thermodynamic properties of the system with constant N and T are obtained from its canonical partition function (CPF), Q_N. The Helmholtz free energy (F) reads

$$F = U - TS = -\beta^{-1} \ln Q_N, \tag{1}$$

where the inverse temperature is $\beta = 1/kT$, k is the Boltzmann constant, U is the system energy, and S its entropy. The reversible work done at constant temperature to change the cavity radius between states a and b is

$$F_b - F_a = -\int_a^b P_w dV, \tag{2}$$

with $dV = A\, dR_{\text{eff}}$. Here, P_w is the pressure on the spherical wall which is an equation of state (EOS) of the system. The derivative of Eq. (2) at constant T gives the pressure on the wall through

$$P_w = -A^{-1} dF/dR_{\text{eff}}, \tag{3}$$

which meets the exact relation known as contact theorem,[40,41]

$$\beta P_w = \rho\,(R_{\text{eff}})\,. \tag{4}$$

In this ideal gas-like relation, $\rho\,(R_{\text{eff}})$ is the value that takes the density profile at contact with the wall. This extended version of the contact theorem for planar walls applies to curved walls of constant curvature (spheres and cylinders), for both open and closed systems. A complete discussion of the presented statistical mechanical approach for few-body confined system that includes other properties, such as the energy, may be found in Refs. 10 and 30.

Here we consider the confined colloids as particles that interact through the square well potential,

$$\phi_{\text{SW}}(r) = \begin{cases} \infty & \text{if } 0 < r < \sigma, \\ -\varepsilon & \text{if } \sigma < r < (1+\lambda)\,\sigma, \\ 0 & \text{if } r > (1+\lambda)\,\sigma, \end{cases} \tag{5}$$

where $\varepsilon > 0$. In this work, we study the short-range SW system with $\lambda = 0.1$. The bulk and interfacial properties of short-range SW fluids have been studied elsewhere.[16,19,24,39] For reference, we note that the bulk SW system with $\lambda = 0.1$ has a metastable fluid-vapor transition with critical temperature $T = 0.47\,\varepsilon/k$ and density $\rho = 0.47\,\sigma^{-3}$.[21,39]

This article is copyrighted as indicated in the article. Reuse of AIP content is subject to the terms at: http://scitation.aip.org/termsconditions. Downloaded to IP: 168.96.66.153 On: Tue, 30 Jun 2015 17:10:17

A. Statistical mechanics of the semi-grand canonical confined AO system

In the AO model, a particular colloid-polymer mixture is characterized by the ratio $q = \frac{\sigma_p}{\sigma}$. The diameter of the polymer coil is given by $\sigma_p = 2R_g$ with R_g the radius of gyration of the polymer. The effect of temperature on R_g was studied in Ref. 42. In the AO model, the temperature does not play any relevant role and thus we consider T fixed to fix σ_p. We consider the mixture of N colloidal particles and polymers at chemical potential μ_p, at a given temperature. The spherically confined system of colloids is such that the polymers, which are much smaller than colloidal particles, can freely pass through the semipermeable wall that only constrains the colloids into the pore. The colloid-polymer AO mixture is an inhomogeneous system that can be analyzed in the semi-grand canonical ensemble. Its partition function is

$$\Xi_m = \frac{\Lambda^{-3N}}{N!} \sum_{N_p} \frac{z_p^{N_p}}{N_p!} Z_{N,N_p}, \tag{6}$$

with $z_p = \Lambda_p^{-3} e^{\beta\mu_p}$, Λ_p the thermal de Broglie length of the polymer and Λ the same magnitude for the colloidal particle. Z_{N,N_p} is the configuration integral (CI) of the mixture with the N colloids, whose centers are constrained to the pore with volume $V = 4\pi R_{\text{eff}}^3/3$, and the N_p polymers in the larger volume V_p. In the Appendix it is shown that Eq. (6) transforms to

$$\Xi_m = \Xi_p \frac{\Lambda^{-3N}}{N!} e^{-\left(\rho_p v_{exc} N\right)} Z_N^{(\text{AO})}, \tag{7}$$

where Ξ_p and ρ_p are the partition function and the mean number density of the pure (homogeneous) polymer system, respectively. $Z_N^{(\text{AO})}$ is the CI of N confined colloids interacting through the effective pair-potential ϕ_{AO} and v_{exc} stands for the excluded volume defined in the Appendix. Given two colloids at a distance r apart, $\phi_{\text{AO}}(r)$ is infinity for $r < \sigma$ and it is zero for $r > \sigma(1+q)$. In the attractive well region $\sigma < r < \sigma(1+q)$, it is

$$\beta\phi_{\text{AO}}(x) = -\eta_p\left(1+q^{-1}\right)^3\left[1 - \frac{3x}{2\left(1+q\right)} + \frac{x^3}{2\left(1+q\right)^3}\right], \tag{8}$$

where $x = r/\sigma$ and $\eta_p = \rho_p\left(\pi\sigma_p^3/6\right)$ is the packing fraction of the polymers (note that η_p takes any positive value). The expression in Eq. (8) is minus ρ_p times the volume of intersection of two spheres of radius $\sigma\left(1+q\right)/2$ whose centers are at a distance r.

For the thermodynamic analysis of the AO model, we use as reference the pure polymer system (an ideal-gas) with the grand-free energy given by $\Omega_p^h = U_p^h - TS_p^h - \mu_p N_p^h$ (with $N_p^h = \rho_p V_p$). The semi-grand free energy of the mixture is $\Omega_m = U_m - TS_m - \mu_p N_p$ and given that the system is athermal, its energy is purely kinetic $U_m = \frac{3}{2}kTN + \frac{3}{2}kTN_p$. We define

$$\begin{aligned} F_{\text{AO}} &= \Omega_m - \Omega_p^h, \\ &= U_c - T\left(S_m - S_p^h\right) + \left(3kT/2 - \mu_p\right)\Delta N_p, \end{aligned} \tag{9}$$

with $U_c = \frac{3}{2}kTN$, $\Delta N_p = N_p - N_p^h$, and $\Omega = -\beta \ln \Xi$. Here, F_{AO} is the free energy of the confined colloids in the polymer solution as an excess over the pure polymer system. The pressure exerted by the colloids on the wall, the osmotic pressure, is

$$P_w = -A^{-1} dF_{\text{AO}}/dR_{\text{eff}}, \tag{10}$$

and relates with the colloids density distribution $\rho(\mathbf{r})$ through the contact theorem,

$$\beta P_w = \rho\left(R_{\text{eff}}\right). \tag{11}$$

Eqs. (10) and (11) are essentially the same as Eqs. (3) and (4) but the meaning of each magnitude corresponds to different systems.

B. Extended law of corresponding states

The short range SW potential and its capability to describe any short range potential (*universality*) was proposed by Noro and Frenkel in their extended version of the corresponding state law.[38] It is based on a mapping between different systems using three parameters: the effective hard core diameter, the well depth, and the adimensional second virial coefficient. The latter was proposed as a measure for the range of the attractive part of the potential. The scheme was used previously for studying the critical properties of the liquid-vapor transition for interaction models including Lennard-Jones and Hard-Yukawa.[38,43,44] Recently, it was employed to analyze the behavior of proteins in water solutions.[39]

It is important to note that we apply the law of corresponding states to analyze confined systems composed of few particles. This is very unusual and thus we made some checks to validate the overall approach that will be shown in Sec. IV. Our application of the law for hard-core systems is based on the use of two natural scales: the hard core diameter for the length scale and the depth of the attractive well for the temperature scale. The reduced second virial coefficient is given by $B = -\frac{1}{2b_2}\int\left[\exp\left(-\beta\phi(r)\right) - 1\right] d\mathbf{r}$ with $b_2 = 2\pi\sigma^3/3$. For the SW system, this gives explicitly,

$$B_{\text{sw}} = 1 - \left(e^{1/T^*} - 1\right) 3\lambda\left(1 + \lambda + \lambda^2/3\right), \tag{12}$$

where we have introduced the adimensional temperature $T^* = Tk/\varepsilon$ (its inverse is $\beta^* = 1/T^*$). In the limit of a very narrow well, the SW potential reaches the Baxter's sticky spheres limit with

$$B = 1 - 1/4\tau.$$

Here, τ (that grows monotonically with T) plays the role of temperature.[45,46] In the AO model, the effective colloid-colloid second virial coefficient B_{AO} is not analytically integrable. To relate B_{sw} with B_{AO}, we link the width of the wells by $q = 2\lambda$. This mimics the fact that $\beta\phi_{\text{AO}}(x)$ is deeper near the hard-core of the particle. For the AO system with corresponding well range $q = 2\lambda$, the relation $B_{\text{AO}}\left(\eta_p, q = 2\lambda\right) = B_{\text{sw}}\left(T^*, \lambda\right)$ fixes the pair of equivalent states $T^* \longleftrightarrow \eta$. This mapping allows the numerical evaluation of B_{AO} and the fit of a nearly linear relation between $1/T^*$ and η for several values of λ. The coefficients obtained for the fitted function

$$\frac{1}{T^*} = \frac{2}{3}\left(1 + 1.5q^{-1}\right)\sum_{i=1}^{3} c_i h_i, \tag{13}$$

This article is copyrighted as indicated in the article. Reuse of AIP content is subject to the terms at: http://scitation.aip.org/termsconditions. Downloaded to IP: 168.96.66.153 On: Tue, 30 Jun 2015 17:10:17

TABLE I. Fitting parameters for the SW-AO mapping. They relate T^* of the SW system to the value of the packing fraction η_p (see Sec. II A) in the corresponding state of the AO system.

$q = 2\lambda$	c_1	c_2	c_3
0.2	0.886 964	0.22 724	0.015 641
0.15	0.884 047	0.29 956	0.013 871
0.1	0.876 335	0.44 847	0.012 614
0.05	0.847 353	0.92 875	0.013 498

with $h_1 = \eta_p$, $h_2 = \eta_p^2$, and $h_3 = \eta_p/(0.1 + \eta_p)$, are shown in Table I. The cases $\lambda = 0.1$ and $q = 0.2$ are presented in Table II, where corresponding values of sticky temperature, adimensional temperature of the SW system, and polymer packing fraction are shown. In Fig. 2, we present the SW potential and the effective AO potential that yields corresponding states for several temperatures and polymer packing fraction ($\lambda = 0.1$ and $q = 0.2$). The inset shows the simple relation between the temperature of the SW particles and the corresponding packing fraction of polymers for the AO colloid-polymer mixture expressed in Eq. (13). In Sec. IV, the overall approach will be used to analyze the spherically confined system of few colloids in a colloid-polymer mixture.

III. SIMULATION METHOD

The system of few colloids modeled as SW interacting particles (without polymers) was studied using molecular dynamics. The statistical mechanical equivalence between different ensembles does not apply to few-body systems. Therefore, simulation and statistical mechanical approaches should correspond to the same physical constraints, to ensure comparable results. In this work, we focus on a system at constant temperature, fixed volume, and number of particles. It corresponds to a canonical ensemble, and thus one assumes a Maxwell-Boltzmann velocity distribution. Accordingly, the simulations have to include a thermostating mechanism that ensures constant temperature and Maxwell-Boltzmann velocity distribution.

Molecular dynamics simulations of few SW confined in a spherical cavity were performed with a standard event-driven algorithm (EDMD).[19,47] The particles move with rectilinear and constant-velocity dynamics, between events, until momentum transfer happens. In order to discriminate particle-particle collisions, we used the logical structure of

TABLE II. Law of corresponding states for short range potentials of SW and AO types. First column presents the sticky-sphere temperature parameter τ. Second and third columns show the temperature for the SW particles and the corresponding packing fraction of polymer for the AO model, respectively.

τ	T^* (SW, $\lambda = 0.1$)	η_p (AO, $q = 0.2$)
0.0051	0.2	0.81 071
0.0675	0.4	0.43 466
0.1758	0.6	0.29 597
0.3033	0.8	0.22 369
0.4395	1.0	0.17 939
0.5805	1.2	0.14 950

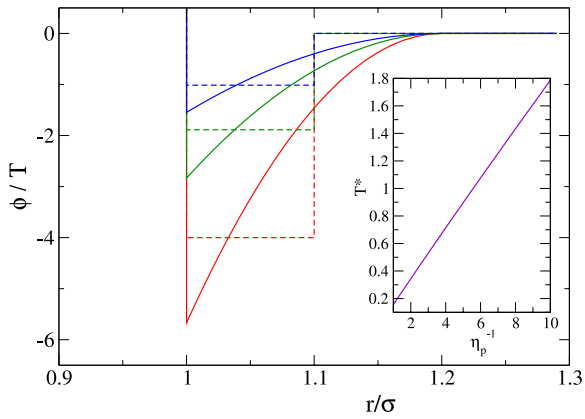

FIG. 2. Corresponding states between SW potential (dashed lines) and AO effective potential (full lines) for $\lambda = 0.1$ and $q = 0.2$. From bottom to top, the inverse of the packing fraction (temperature) for AO (SW) curves is $\eta_p^{-1} = 1.5$, 3, and 5.5 ($T^* = 0.25$, 0.53, and 0.985). The inset presents the nearly linear relation between T^* and η_p used to map the SW system to the AO model.

Alder and Wainwright.[48] Constant temperature was achieved by using a thermal-wall thermostat, which changes the velocity of the particle colliding with the wall by means of a velocity distribution compatible with canonical ensemble for a given temperature T. Thermal walls show certain features different from those thermostats that act over the entire system volume that were discussed in detail in a previous work.[10] The thermal-wall thermostat acts on the colliding particle by imposing it a new velocity, which is chosen stochastically from the probability distributions

$$\begin{aligned} p_n(v_n) &= m\beta|v_n| \exp\left(-\beta\frac{1}{2}mv_n^2\right), \\ p_t(v_t) &= \sqrt{\frac{m\beta}{2\pi}} \exp\left(-\beta\frac{1}{2}mv_t^2\right). \end{aligned} \tag{14}$$

Here, n and t stand for the normal and tangential components of the velocities, that lie in directions $-\hat{r}$ and $\mathbf{v}^{\text{old}} - (\mathbf{v}^{\text{old}} \cdot \hat{r})\hat{r}$, respectively. The thermal walls described by Eq. (14) were tested for HS confined both by planar walls and in a spherical pore, and produce a velocity distribution compatible with that of Maxwell-Boltzmann.[10,49] We get the same results for simulations with SW particles.

Setting an N value between 2 and 6, we swept the (T, ρ) surface. For each chosen point of that surface, we performed 10 simulations of 3×10^6 collision events. Temperature range was chosen to include two regions of distinctive behavior. At low T, particles rack up and form a cluster that acts as a rigid body, at high values particles dissociate resembling a HS system. Densities were picked from the very low "bulk like" to high values, in the vicinity of close-packing condition.

From simulations, we get to measure several quantities attained from time averages over all systems' configurations. The studied structure and position functions are: the one body density function $\rho(\mathbf{r})$ and the *averaged* pair distribution function $\bar{g}(r)$.[30] The upper bar is just to distinguish our measured function from the better known radial distribution function $g(r)$ that is commonly used to study homogeneous and isotropic systems. The calculated profiles for $\rho(r)$ and $\bar{g}(r)$ are mean values over a discrete domain, obtained from

This article is copyrighted as indicated in the article. Reuse of AIP content is subject to the terms at: http://scitation.aip.org/termsconditions. Downloaded to IP: 168.96.66.153 On: Tue, 30 Jun 2015 17:10:17

a binning of spherical shells during the elapsed simulation time. The bin length is established by dividing the maximum possible distance value (R_{eff} for $\rho(r)$ and $2R_{\text{eff}}$ for $\bar{g}(r)$) by the number of desired bins, usually 1200.

IV. RESULTS

In this section, we present the properties for the confined system of few short-range SW particles ($\lambda = 0.1$) obtained from the molecular dynamics simulation. They are separated in structural properties, thermodynamic observables, and phase diagram. Structural behavior is analyzed in terms of the spatial correlation between particles from $\bar{g}(r)$ and their spatial distribution in the cavity from $\rho(\mathbf{r})$. The measured thermodynamic quantities describe the system as a whole, focusing on magnitudes that are usually utilized to characterize both bulk and inhomogeneous fluids in the thermodynamic limit. The statistical mechanical background was developed in Sec. II and in Ref. 30. Phase diagrams should not be understood in the context of bulk phases. Even, they condense the observed system behavior in the temperature/density plane. For simplicity, all the magnitudes are presented using natural units, i.e., the unit of length is σ, the unit of temperature is k/ε, and the unit of energy is ε.

Additionally, we discuss to which extent we expect an accurate mapping of different structural and thermodynamic properties between the simulated short-range SW system with $\lambda = 0.1$ and the AO system with $q = 0.2$. We analyze some properties of the equivalent AO system based on the mapping between T and the packing fraction η_p. The application of the extended law of corresponding states between the AO and the SW confined systems is tested in Subsection IV C.

A. Structural description

We present first the results for the $N = 2$ system, from which, exact theoretical results are available.[30] This allows us to make a direct comparison between exact predictions and simulation results. By getting a perfect matching, we ensure that we have solid framework to analyze the few-particle systems of higher N. It is also useful for validating the simulation program and thermostating procedure. The pair distribution function is shown in Fig. 3 for different temperatures. A clean superposition between theory and simulation is easily appreciable. For $N = 2$ the analytic form of $\bar{g}(r)$ is

$$\bar{g}(r) = Ce_{12}(r)\left[(2R_{\text{eff}} - r)^2(r + 4R_{\text{eff}})\right], \qquad (15)$$

with $e_{12}(r) = e^{-\beta\phi(r)}$ and $C = \frac{\pi}{12Z_2}$.[30] First, the vanishing values in the range $0 < r < 1$ are a trivial effect of the hard core repulsion. Then in the range $1 < r < 1.1$, there is always a main peak. This peak is an expected result, given the shape and length of the potential: inside the well attractive zone, particles are more likely to be closer. Another common element of these curves is the presence of "tails," i.e., the smooth monotonically decreasing segments that are seen for ranges of r beyond the main peak. The tail ends at $2R_{\text{eff}} = 1.97$ (cavity diameter) which is the maximum possible pair distance. Since there is not particle interaction for pair distance over 1.1, the tail is proportional to the probability of finding a pair of hard spheres at a given distance, in spherical confinement. The relation between the main peak and the tail sizes is driven by the temperature: a steep jump in e_{12} will happen at low T, and e_{12} approaches to unity at high T. From a phenomenological standpoint, at low T the particles lack the energy to escape from the well, thus forming a permanent short ranged bond. At high T, the kinetic energy is far greater than the well depth, meaning that the system resembles one of colliding hard cores (HS limit). For higher N, the competition between the structure (peaks) and the tail (no interaction) is one of the most visible effects while changing T.

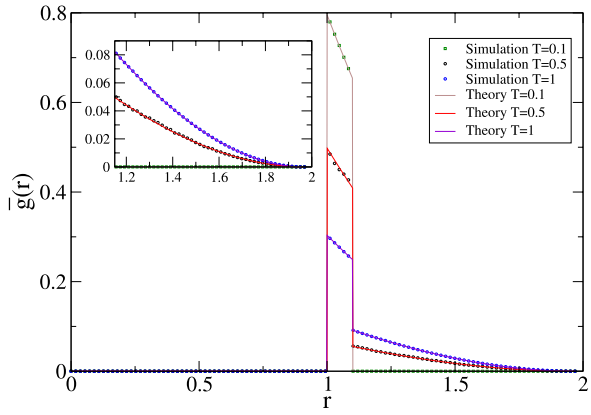

FIG. 3. Pair distribution function curves for $N = 2$ and $\rho = 0.5$ for different temperatures. A clear agreement between theoretical and simulation results is observed. The inset shows same curves on the range $r \in [1.15, 1.97]$.

As regards the behavior of an equivalent AO system, the relationship between the pair correlation functions $\bar{g}_{\text{sw}}(r)$ and $\bar{g}_{\text{AO}}(r)$ was not studied for confined systems, to the best of our knowledge. However, based on our analysis of the case $N = 2$, we propose that the corresponding functions are $\bar{g}_{\text{sw}}(r)/e_{12}^{(\text{sw})}(r)$ and $\bar{g}_{\text{AO}}(r)/e_{12}^{(\text{AO})}(r)$, with $r > 1$. This mapping produces small changes in the shape of the main peak of $\bar{g}_{\text{AO}}(r)$ in comparison with $\bar{g}_{\text{sw}}(r)$.

As can be seen in Fig. 4, where the pair distribution function for 3–6 particles inside the cavity is shown, adding

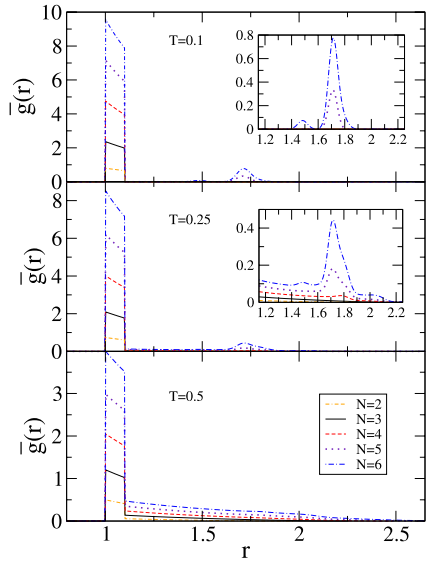

FIG. 4. $\bar{g}(r)$ curves for $N = 2$–6 at fixed number density $\rho = 0.5$. Chosen temperatures are (top to bottom in order) 0.1, 0.25, and 0.5. The insets present the second neighbour peak in more detail.

This article is copyrighted as indicated in the article. Reuse of AIP content is subject to the terms at: http://scitation.aip.org/termsconditions. Downloaded to IP: 168.96.66.153 On: Tue, 30 Jun 2015 17:10:17

particles to such a small system will necessarily cause qualitative changes beyond the two-body analysis. Nonetheless, certain central aspects related to the potential shape remain the same, such as the main peak and the HS limit. Since the integral over the complete space of $\bar{g}(r)$ is $N(N-1)/2$,[30] it is expected that lower N (at fixed ρ) shows overall lower curves. Given that $R_{\text{eff}} = (3N/4\pi\rho)^{1/3}$, at low N values and fixed number density, cavity size is highly susceptible to the addition or subtraction of a single particle. The shape of $\bar{g}(r)$ for different temperatures can be used to provide qualitative aspects of the morphology of the clusters. For very low temperatures ($T < 0.1$) the particles form a rigid cluster, minimizing the overall system energy. Every close neighbor ($1 < r < 1.1$) adds up $-\varepsilon$ to the potential energy. The bonds are mainly permanent, meaning stable pair distances leading to clearly discernible peaks.

For these few-particle systems, it is possible to interpret the low T curves $\bar{g}(r)$, by considering the average cluster shapes. Three particles form a triangle and four a regular tetrahedron (see Fig. 5(a)), both of which have in common that all the particles are first neighbors among themselves. This means that the whole probability of finding a pair at certain distance will localize in the first neighbor range of the pair distribution function (main peak). This isolated peak is shown for $N = 2$–4 in Fig. 4, top panel.

The shape of $\bar{g}(r)$ for $N = 5$ can be understood starting from the $N = 4$ regular tetrahedron and then adding an extra particle on one of its faces, shown in Fig. 5(b). The resulting structure has three particles, each one with four first neighbors and two particles with three first neighbors and one second neighbor. A cluster geometry with second neighbors gives rise to a non-vanishing probability of finding a pair distance larger than the main peak region. The stable structure, with the second neighbor distance in a constrained region, results in a second peak.

For the case $N = 6$ there are two observed cluster geometries. One of them is the regular octahedron, presented in Fig. 5(d). However, the most frequent geometry observed in the simulations is the irregular octahedron shown in Fig. 5(c). This irregular polyhedron has a typical path of formation starting from a hexahedral cluster of five particles to which the remaining particle adds over one of its faces. For extremely low temperatures ($T \ll 0.1$), once the particles form their bonds, they will stay bonded permanently. For a softer cluster ($T \lesssim 0.1$), single bonds have a slight chance of breaking and a rearranging of the cluster structure can take place. The secondary peak of $\bar{g}(r)$ is sensitive to these different structures as shown in the inset of the top panel in Fig. 4. There are two secondary peaks related to second neighbor distances: the larger one represents the second neighbors in the irregular octahedron, while the smaller one is characteristic of the regular body. The significant height difference shows that the irregular cluster is much more likely. We point out also that both geometries have the same number of first neighbors thus being isoenergetic. Therefore, from a statistical mechanics point of view, the only factor that can lead to the prevalence of one geometry over the other one is strictly coming from entropic contributions. The irregular cluster presents lower symmetry and higher entropy.

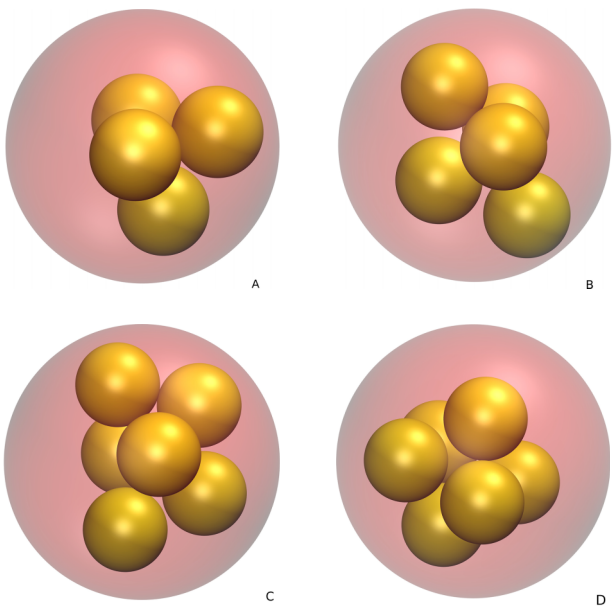

FIG. 5. Clusters with different shapes for $N = 4$–6. Configurations were obtained from simulations at $\rho = 1$ and $T = 0.15$.

Increasing the temperature further leads to the break up of multiple bonds, which results in flexible or plastic clusters. For intermediate T ranges ($0.1 < T < 0.25$), the particles remain linked, but they are not tightly bonded. Certain bonds are likely to break, enabling the particles to displace inside the cluster. The inset of Fig. 4 shows that the isolated peaks are surrounded by non-vanishing values of $\bar{g}(r)$. For example, the triangle for $N = 3$ breaks one of its pair bonds opening up and stretching like a chain. For higher N, is essentially the same. Additional translational freedom leads to possible deformations into wider shapes than the original rigid body. The weaker the structure is, the lower the main and second peaks become increasing $\bar{g}(r)$ on the surrounding areas.

For higher temperatures ($T > 0.3$), soft clusters start to dissociate and single particles are free to have any distance from the cluster, inside the cavity limits. Any kind of stable structure fades out and only instantaneous pairs endure. As can be seen in the bottom panel of Fig. 4, the tail engulfs any close range structure and the main peak reduces around half of its height, compared to the $T = 0.25$ panel. Higher temperatures do not add any qualitative variation: the main peak will decrease until it becomes part of the tail, in the HS limit.

Density profiles, shown in Fig. 6, present very explicitly the inhomegeneity of the system. Unlike commonly studied bulk systems, there are significant local spatial variations of the one body density function. Note that $N = 4\pi \int_0^{R_{\text{eff}}} \rho(r) r^2 dr$ and thus R_{eff} varies with N in Fig. 6. It takes values from $R_{\text{eff}} = 1$ for two particles up to $R_{\text{eff}} = 1.9$ for six particles. For the case $N = 2$, the density vanishes in the center, because if one particle is placed at $r \approx 0$, the available volume for the other one becomes very small. For density values that define effective radii higher than the particle diameter, for the cases $N = 3$–6, all the profiles have similar form, independent of particle number. The profiles have two distinct regions. An approximately constant density on the center of the cavity, that is cut at the vicinity of the wall ($R_{\text{eff}} - r < 1$), and the "interfacial" region closer to the wall. The extension of the plateau depends

This article is copyrighted as indicated in the article. Reuse of AIP content is subject to the terms at: http://scitation.aip.org/termsconditions. Downloaded to IP: 168.96.66.153 On: Tue, 30 Jun 2015 17:10:17

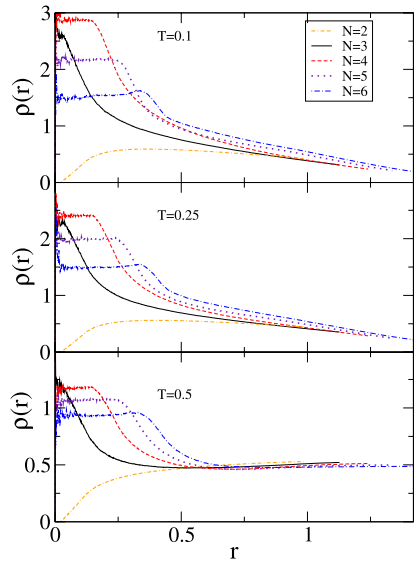

FIG. 6. Density profiles for $N = 2$–6 at fixed number density $\rho = 0.5$. The chosen temperatures are (top to bottom in order) 0.1, 0.25, and 0.5.

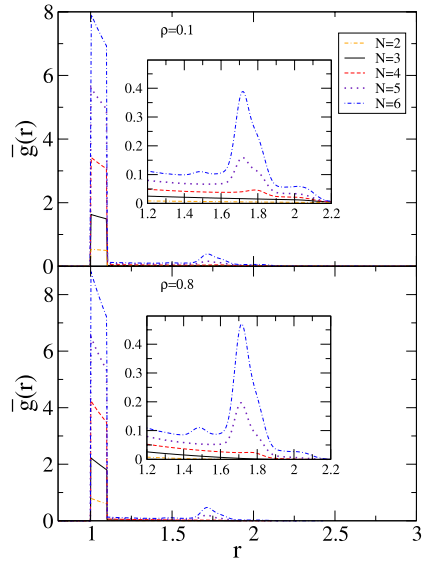

FIG. 7. $\bar{g}(r)$ curves for $N = 2$–6 at fixed temperature $T = 0.25$. Number densities are 0.1 (top) and 0.8 (bottom). The insets present the second neighbour peak in more detail.

on the relation of cavity size and particle diameter, as observed from the different sizes at equal number density in Fig. 6. For low temperatures the system may be treated as a single nearly rigid body, free to translate and rotate in the central region. When the cluster gets closer to the wall, some possible cluster orientations are restricted, leading to a reduction in rotational entropy. Consequently, it is more likely to find the cluster in the central region. Higher temperatures soften the particles' bonds progressively, causing a reduction of the disparity between the plateau and the region close to the wall. Once dissociation becomes dominant for high temperatures, depletion arises and the wall has a higher effective attraction. Further increase in the temperature makes the wall attraction higher, while the particle correlation disappears. At the HS limit, the highest probability of finding a particle is at the wall. This was also observed in a system of pure HS particles in spherical confinement.[10] For the AO system we expect similar density profiles to those of SW for equivalent temperature and packing fraction. The temperatures $T = 0.1$, 0.25, and 0.5 correspond to (top to bottom panels in Fig. 6) polymers' inverse packing fraction $\eta_p^{-1} = 0.694$, 1.50, and 2.84, respectively. As we will see, the case $T = 0.1$ may be a low temperature to use the extended law of corresponding states.

The structure dependence on ρ is far more subtle than on T. In Fig. 7, curves of $\bar{g}(r)$ at $T = 0.25$ and for two different densities are shown. One observes that the shape of the peaks remains practically unaltered. Global values of the curve rise for higher number densities, because the normalization is the same in a smaller cavity size. The same general picture was observed for other values of T, not shown here.

From here on, we select the case $N = 5$ to give more detailed analysis. This case is the only one that presents a second peak but does not have multiple stable geometries, as the case $N = 6$. At low temperatures a clearly defined structure is observed, while retaining a little longer range order. The $N = 5$ results can be extrapolated to the other few-particle systems. Density profiles are shown in Fig. 8 for a wide range of temperatures and number densities. As already pointed out, at low and intermediate densities there exist a plateau and an interfacial region close to the wall. Increasing the temperature leads to an overall probability density favoring position closer to the wall, as a result of relatively stronger depletion attraction.[10,50] The higher the density, the smaller the available free volume for the rigid cluster, thus the plateau becomes smaller and steeper. At a certain number density, there is no more room to locate a particle in the center of the cavity. The available space is so small that a particle at the center would push the remaining ones out of bounds. This is shown in the lower panel of Fig. 8, which exhibits an excluded volume region, close to the center of the cavity. This gives a clear insight of how the system conformation and translation become dominated by the cavity shape, at high densities. Rigid clusters have low translational freedom and therefore their

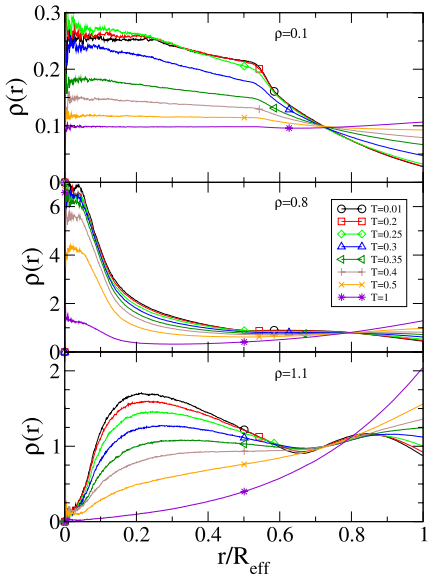

FIG. 8. Density profiles for $N = 5$ at different temperatures. Number densities are 0.1 (top), 0.8 (center), and 1.1 (bottom).

This article is copyrighted as indicated in the article. Reuse of AIP content is subject to the terms at: http://scitation.aip.org/termsconditions. Downloaded to IP: 168.96.66.153 On: Tue, 30 Jun 2015 17:10:17

constituent particles stand at approximately fixed distances from the center. Cluster structure gets expressed on the density profiles that show local maxima and minima. Increasing the temperature softens the cluster, causing the smoothing of the local structure and leaning towards monotonous curves. Finally, at dissociation temperatures, the depletion dominance gets clear and the density at the wall is the highest in the profile. We note here a difficult related to the spherical shape of the cavity: the local properties are hard to measure in the central region because it is poorly sampled. Indeed, the sampling becomes poorer as r decreases towards the center of the pore. This effect is produced by the rapid reduction of the sampled volume, that produces large fluctuations in $\rho(r)$ and other quantities. These fluctuations can also be observed in Fig. 6.

In Figure 9, a similar systematic approach is applied for $\bar{g}(r)$, under density variation. Each studied density $\rho = 0.1$, 0.8, and 1.1 corresponds to a cavity diameter of 4.57, 2.28, and 2.05, respectively. By increasing the temperature, pair bonds are more likely to break and produce dissociations. The odds of a separated pair to rebond are smaller at larger free space. As a consequence, main peaks fall more abruptly at dissociation temperatures and lower densities. At high densities, there is not enough room for the particles to stay away from each other, which forces an increase in the probability of finding pair separations inside the well range, even if particles have a very high kinetic energy, as compared to the well interaction energy ε. At $\rho = 1.1$ it is noticeable how cavity diameter is close to second neighbor distance. For $N = 5$, the rigid cluster geometry is also the most compact that the system can achieve. The cavity is only slightly larger than the smallest possible configuration. This implies that the entire cluster is practically locked in the center, allowed mostly to rotate. As already observed in Figure 8, at high densities and low temperatures, the particles of the rotating rigid body maintain a stable distance from the center. For $\rho > 1.1$, the wall cavity squeezes the system, shortening the second neighbor distance.

Despite the SW interaction being isoenergetic once inside the field range, the main peak of $\bar{g}(r)$ shows a negative slope as can be observed in Figs. 3, 4, 7, and 9. This implies that, within the interaction range $r \in [1, 1+\lambda]$, particles tend to be at closest distance instead of near the external side of the well. Theoretical results for $N = 2$ (Eq. (15)) indicate that the slope originates from the particle-cavity interaction. The main peak is basically an offset mounted on a decreasing function. This can be rationalized by noting that a closer pair has more free space in the cavity than a stretched one, increasing the translational entropy. In addition, collisions with a curved concave wall tend to aggregate the particles, in average.

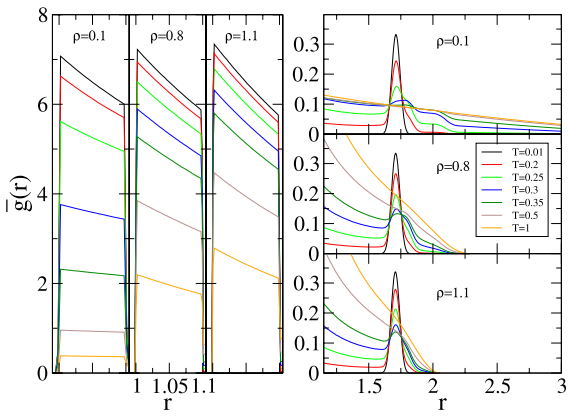

FIG. 9. $\bar{g}(r)$ for $N = 5$ at different temperatures and representative number densities. Left panel: details of the main peak, right panel: details of the second peak for $r \in [1.15;3]$.

B. Thermodynamic quantities

We focus on four thermodynamic properties to characterize the system as a whole. We analyze pressure and energy, that have robust definitions and are measured in a straightforward way. Additionally, we study the surface tension and the surface adsorption, which are intrinsically related with the inhomogeneous nature of the system. These last quantities are more subtle and difficult to measure by simulation.

Pressure on the wall is expected to increase with temperature and number density, given that both parameters should increase the average number of collisions on the wall. We work with the compressibility factor $\beta P_w/\rho$ in Fig. 10 to eliminate the linear dependence, allowing to distinguish deviations from the ideal case $\beta P_w/\rho = 1$. Only the high temperature and very low density cases follow the ideal behavior, when the relative well attraction is too weak and excluded volume from the cores is negligible. Cluster to dissociation temperatures are mediated by a sudden increase in $\beta P_w/\rho$ and further saturation. The jump becomes smoother for higher densities as a result of what has been pointed out from $\bar{g}(r)$ analysis: with less space for separation, qualitative differences between a cluster and unbounded particles are smaller. The emergence of depletion, for any density value at high T, explains the asymptotic increase of $\beta P_w/\rho$ until the HS limit.

At very low temperatures, the system is far away from the ideal gas behavior because the relatively deep potential well produces a cluster. In this limit, the system's compressibility factor increases monotonically for increasing density. We attribute this to the behavior of a unique finite-size cluster confined in an effective volume $V_{\text{cluster}} < V$. The single cluster

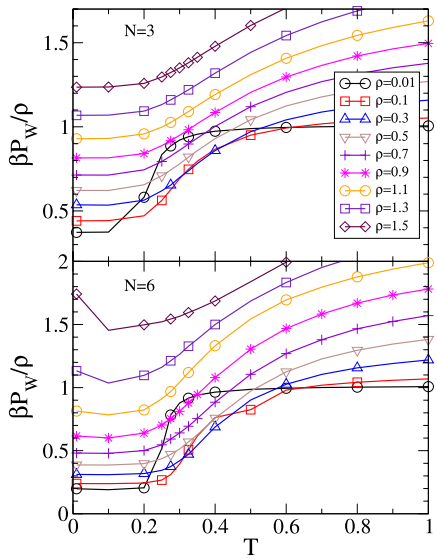

FIG. 10. Compressibility factor $\beta P_w/\rho$ as a function of temperature, for different number densities for $N = 3$ (top panel) and $N = 6$ (bottom panel).

This article is copyrighted as indicated in the article. Reuse of AIP content is subject to the terms at: http://scitation.aip.org/termsconditions. Downloaded to IP: 168.96.66.153 On: Tue, 30 Jun 2015 17:10:17

behaves as an ideal gas, and thus, its compressibility factor is $\beta PV_{\text{cluster}} = 1$, i.e., $\beta P/\rho \simeq N^{-1}V/V_{\text{cluster}}$. This explains the low-density and low-temperature values $\beta P_w/\rho \gtrsim 0.33$ and $\beta P_w/\rho \gtrsim 0.17$ for $N = 3$ and 6, respectively. At intermediate temperatures, when the bond-breaking probability is non-negligible, the cases of low density rise much more rapidly to its saturation value than those of higher densities. This could be related to the strong reduction of recombination rate at lower densities. Once a bond is broken, the probability of the particles to meet again is very small. This is not the case for intermediate to high densities.

The mean energy per particle E is the addition of the kinetic term $3T/2$, driven by the temperature and the mean potential energy. For low temperatures, where $|\phi_N|/N \gg 3T/2$, the system is in a rigid cluster state. Then, E can be precisely calculated as the number of bonded pairs for a given geometry. We call that value cohesion energy E_{coh}, which is the lowest (fundamental) possible energy of the system and we define it as the zero value in Fig. 11, presenting the energy versus temperature. Average energy per particle has a similar behavior to that of the pressure in Fig. 10. For low density, it presents an abrupt increment in going from low to higher temperatures ($T \sim 0.2$). This jump agrees with the range of non-rigid cluster, ending at dissociation temperatures ($T \sim 0.3$). It then follows a weak linear variation for high temperatures, according to the equipartition theorem. It is worth noting that for systems with a unique stable rigid cluster geometry at low temperatures, all the curves must collapse to a single one with slope 3/2, independent of the density. For reference, the kinetic energy and a shifted energy ($E_{kin} + |E_{\text{coh}}|$) are also shown in Fig. 11, in dotted and dotted-dashed lines, respectively. Rigid clusters constitute compact structures, and increasing the density does not change the number of first neighbors. Higher density lines have lower values, because the particles are closer, so SW interactions are forced. The changes produced with increasing temperature in each curve are more pronounced for higher N, because the rigid cluster has more bonds (per particle) to be broken. This feature is also shown for the different values that take $|E_{\text{coh}}|$, in dashed line. The line also serves to visualize the condition $E = 0$, which characterizes the equilibrium between potential and kinetic energies. This crossover line separates two characteristic regions: one, below the line, where the potential energy dominates over the kinetic energy, proper of clusters. Above the line, kinetic energy dominates, a feature proper of gases.

Surface adsorption Γ and surface tension γ are basic properties used to characterize the inhomegeneity induced on the system by the presence of walls. They are measured in the same way, in a previous work.[10] We will not delve into details and only give here the definition of Γ, and the expression of γ, based on Laplace equation: $\Gamma = (\rho - \rho_c)\frac{V}{A}$ and $\gamma = \frac{P_c - P_w}{2} R_{\text{eff}}$. Here, ρ_c (P_c) refers to the average density (pressure) near to the center of the cavity. These magnitudes are difficult to measure because one must fix a criterion to choose the region where averages should be taken. The criterion must be applied for all the available ranges of ρ and T. Note that at large R_{eff}, the density profiles attain a nearly constant value in the central region (*plateau*). At constant N, the density ρ_c becomes higher for smaller cavity radius until a limiting value, in which particles cannot freely place themselves in the center. This central region progressively turns into an excluded zone. It is important to note that at such high packing values, the definition of ρ_c is less accurate, since there is no clear distinction between the center region and that in the vicinity of the wall. Adsorption is shown in Fig. 12. For low densities, adsorption is negative for small T and then experiences a jump around dissociation temperatures, to flatten at higher values of T. It becomes positive at high temperatures. For high densities, adsorption is positive and nearly independent of the temperature. The limiting cases of temperature are clearly identified. For high temperature, Γ is positive and increases monotonously with the density. In the case of low temperature, for small densities Γ is negative and decreases with increasing ρ, up to a certain minimum value. Further increment of ρ

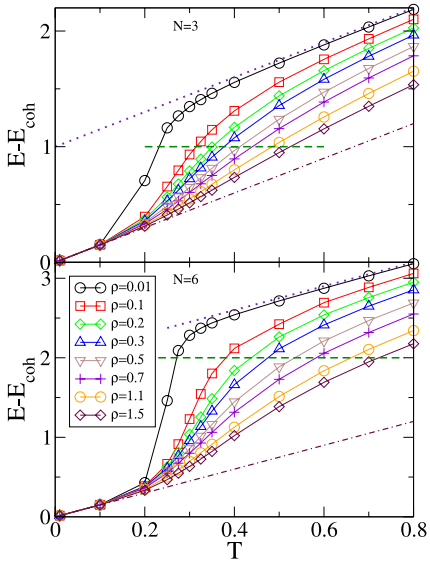

FIG. 11. $E - E_{\text{coh}}$ as a function of T for different number densities. Top panel shows $N = 3$ and bottom panel $N = 6$ cases. The horizontal dashed line plots $|E_{\text{coh}}| = -E_{\text{coh}}$.

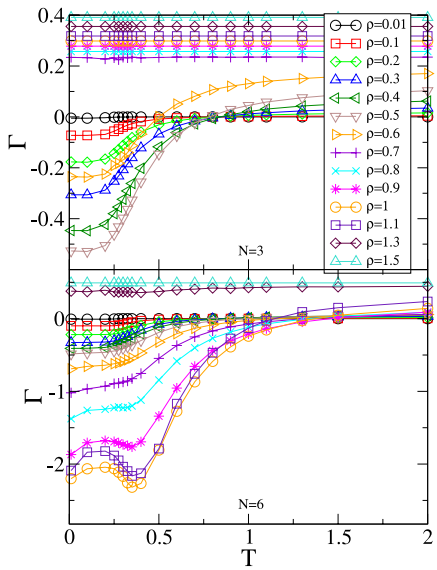

FIG. 12. Adsorption Γ as a function of temperature for different number densities. The cases $N = 3$ (top panel) and $N = 6$ (bottom panel) are shown.

This article is copyrighted as indicated in the article. Reuse of AIP content is subject to the terms at: http://scitation.aip.org/termsconditions. Downloaded to IP: 168.96.66.153 On: Tue, 30 Jun 2015 17:10:17

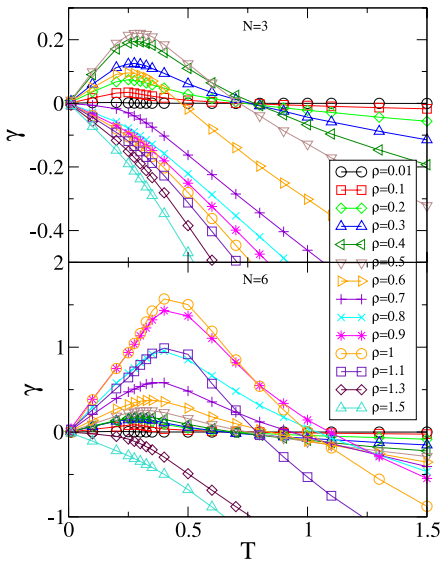

FIG. 13. Surface tension as a function of T for different number densities. The cases $N = 3$ (top panel) and $N = 6$ (bottom panel) are shown.

produces a sudden rise of Γ, which becomes positive. This behavior goes in line with that observed in the density profiles, in Sec. IV A. $\rho(r)$ presents an enhancement close to the wall for $\Gamma > 0$ and an increment in the center for $\Gamma < 0$.

Fig. 13 shows the surface tension γ for three (top panel) and six particles (bottom panel). At vanishing temperature they start from 0, having then two distinctive behaviors. For low to intermediate densities the γ curves are positive at low T. They start with positive slope, reach a maximum value, to become negative at high temperatures. For high densities, γ curves are negative. They start with negative slope and decrease monotonously with temperature.

The two different characteristics of γ can be rationalized by considering that when clusters are favored at medium to low densities, the system tends to get far from the cavity wall, having the cluster size as its characteristic size. This minimizes the intrinsic area of the system, going along with a negative adsorption and an increase of density at the center of the cavity. At high enough temperatures, the system behaves as HS particles, having the confining cavity as a characteristic size, with an effective entropic attraction from the wall, and a negative surface tension.[10] The curve shows that the global maximum of surface tension corresponds to higher density for $N = 6$ than for $N = 3$. Also, the temperature of those global maxima of γ is shifted towards higher values.

The approximate linear dependence of γ with T for both very low and high temperatures is explained by the expected hard sphere limit where $\beta\gamma$ only depends on density. The behavior upon variation of density is similar to that observed for Γ.

Some of the measured thermodynamic properties of the SW system can be readily mapped to the AO model by the established relation between T and η_p. We expect one of these magnitudes to be the pressure on the wall, once the energy scale is compensated [as in the case of $\beta\phi_{AO}$ in Eq. (8)], thus βP_w and also $\beta P_w/\rho$ which was plotted in Fig. 10 could be mapped. The measured surface tension is similar to the pressure, it should be transformed to $\beta\gamma$. A third magnitude is Γ which does not scale with T and depends on characteristic features of $\rho(r)$. The case of energy is more complex because in the AO system the energy is purely kinetic, and therefore the energy cannot be mapped.

C. Phase diagrams

In Fig. 14, we show the change of the main characteristics of the phase diagram with the variation of N. This summarizes variation of structural properties with T and ρ. The vertical lines come from the analysis of the pair distribution function, by comparing the height of the main peak $\bar{g}(r = 1^+)$ with that in the region next to it, $\bar{g}(r = 1.1^+)$, and their connection with the qualitative behavior of the system, obtained by direct visualization of the dynamics of the particles. C corresponds to $\bar{g}(r = 1.1^+)/\bar{g}(r = 1^+) = 0.005$ and D to $\bar{g}(r = 1.1^+)/\bar{g}(r = 1^+) = 0.03$. The relations between those points have been picked by noting that those values match cluster softening (C) and dissociation process (D). These lines divide temperature domains by particle conformation: low temperatures until C, mostly defined by particles forming a hard cluster. Between C and D the system forms a soft cluster with relative movements among particles. For higher temperatures, beyond D, frequent dissociations are observed. The horizontal lines come from the analysis of the main features of the density distribution. Line A indicates the cases in which the density profile at the center of the cavity $\rho(r = 0)$ reaches its maximum, and line B when it becomes zero $[\rho(r = 0) = 0]$. The former case represents low translational freedom for the particle that is at the center, while for the latter there is such a high density (or a small cavity) that a particle cannot be in the center due to the excluded volume. These horizontal lines delimit the following regions: below B there is a zone in which the system is moderately inhomogeneous. The region limited by A and B corresponds to a strong reduction of freedom of motion that reduces the occupation in the center. For densities beyond

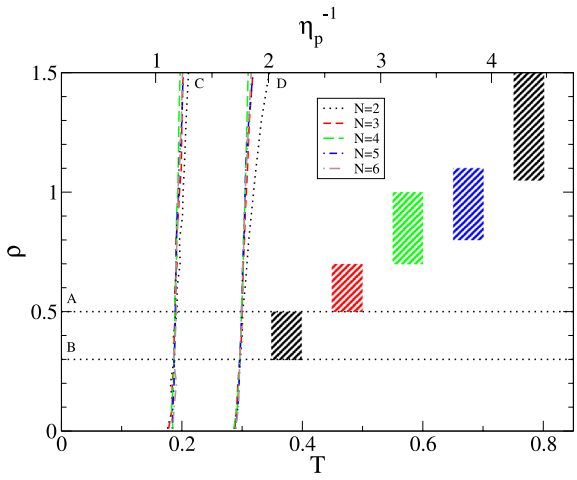

FIG. 14. Superimposed phase diagram for $N = 2$–6. Vertical lines come from analyzing the pair distribution function. At the left side of C there is a hard cluster region. Between C and D we define a soft or plastic cluster region and at the right side of C, dissociation starts to happen. Horizontal lines show density points where density profiles are maximum (B), or vanish at the center (A). The rectangles show the range of ρ between A and B positions for each N value.

This article is copyrighted as indicated in the article. Reuse of AIP content is subject to the terms at: http://scitation.aip.org/termsconditions. Downloaded to IP: 168.96.66.153 On: Tue, 30 Jun 2015 17:10:17

line A, the center of the cavity is an excluded volume (high confinement). Note that a third horizontal line (not shown) fixes the maximum density of the confined system where it becomes completely caged. This density can be calculated with a simple geometrical approach and varies with N. In contrast to the vertical lines, the position of A and B is strongly dependent on N. This is shown with dashed rectangles, whose horizontal sides indicate line A (lower side) and line B (upper side) for the different number of particles.

In Figs. 15–19 we present the phase diagram for the different number of particles studied. A set of characteristic values of density and temperature labeled with letters A–D is shown. They separate regions where the systems present different qualitative behavior. These regions would represent different phases of the system in a macroscopic context.

Additionally, the scalars chosen to distinguish different qualitative behavior of the system are the (T, ρ) points on which: kinetic energy is equal to potential energy (black circles), pressure on the wall follows ideal gas equation of state (red open squares and crosses), adsorption and surface tension change their signs (green diamonds and blue triangles, respectively). We point out that the (T, ρ) grid step is 0.1, except for the cases of low temperatures (e.g., $T = 0.01$) and higher densities where the steps become more spaced. In particular, low temperature $\beta P_w = \rho$ points (red crosses) have been attained by interpolating βP_w curves for specific density values, whose variations are too small for our scale.

The $E = 0$ curve (open circles) divides the phase space. Towards the left, the (modulus of) potential energy is higher than the kinetic energy and the opposite case is true, towards the right. In the region with $E < 0$ (at the left of $E = 0$) the potential energy dominates. This feature is characteristic of systems that spontaneously collapse in cluster aggregates or condensed phases, but also of cold enough compressed systems, where the available space is reduced. On the opposite, when $E > 0$ (at the right of $E = 0$ curve) the kinetic energy dominates and this is typical of systems of free particles, as the case of diluted gases. Note that this last region includes a high enough temperature and high density range, where particles stay together, as a consequence of the strong confinement. The $E = 0$ curve is specially sensitive to changes in N, since it is affected by the average number of bonds per particle. At low N, adding particles increases the maximum number of bonds per particle, given that the system is too far away from bulk case. As a result of this, the curve shifts towards higher temperatures upon increasing N. This is specially observed comparing Figures 15 and 16. The curve flattens for higher densities since smaller cavity forces bond formation, leading to a fixed potential energy value of a tightly packed cluster. This curve has no counterpart for the colloid-polymer mixture analyzed with the AO model. Even when there is an effective potential between colloids, the system is athermal and the origin of the potential is purely entropic. Both colloids and polymers have only kinetic energy, thus $E \neq 0$ for non zero temperatures.

The curve $\beta P_w = \rho$ (open squares) indicates the points of the (T, ρ) where the EOS for the system pressure behaves like the ideal gas pressure P_{id}. At the left side and below the $\beta P_w = \rho$ curve, $P_w < P_{\text{id}}$, the system is undercompressed with respect to the ideal gas (at the same temperature and number density). This region encloses the origin. Outside this region $P_w > P_{\text{id}}$, the system is overcompressed in comparison with the ideal gas. For low densities and high temperatures, this is expected as a consequence of depletion favoring wall contact. Higher densities force wall contact independent of temperature. The theoretical prediction based on the limit of large V (low density) is shown with a red square on T axis. Notably, the obtained limiting temperature 0.7186 fits the curve and is independent of N. From $N = 3$ to 6, all these curves follow a similar behavior: from zero density up to $\rho \approx 1$, where $T \approx 0.3$. The curves at lower temperatures show a strong dependence with N. It is interesting to note that the critical temperature of the vapor-liquid metastable transition in the studied short-range SW system is $T = 0.47$, which, for

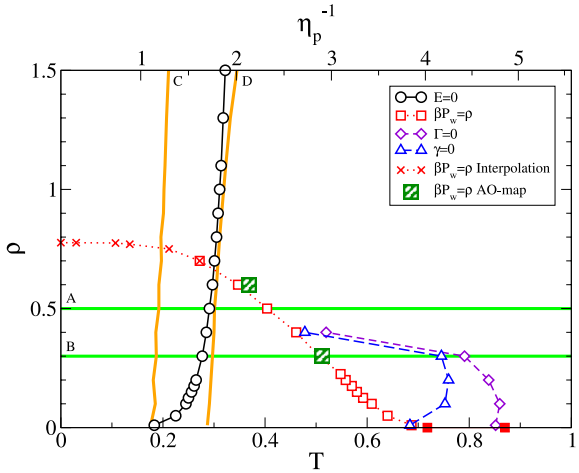

FIG. 15. Phase diagram for $N = 2$ with characteristic curves. A–D thick lines are the same from Fig. 14. Additionally, curves indicating $E = 0$ (black circles), $\beta P_w = \rho$ (open red squares), $\Gamma = 0$ (green diamonds), and $\gamma = 0$ (blue triangles) are shown. Red crosses present the values obtained by interpolating the curves of $\beta P_w/\rho$ for specific density values. These lie between points for which simulation results are available, thus allowing to complete the curve at the saturation area. The two red filled squares show exact analytic values for $\beta P_w = \rho$ and $\Gamma = 0$ at $\rho \to 0$. Green bigger squares represent the AO model results for $\beta P_w = \rho$. In the top x-axis, the scale of packing fraction of polymers in the AO model is presented.

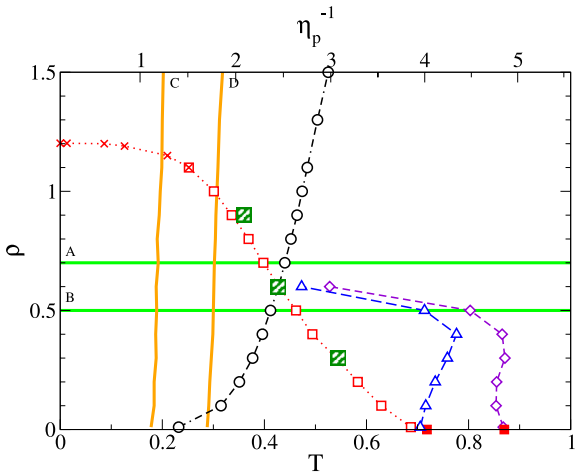

FIG. 16. Phase diagram for $N = 3$ with characteristic curves. Symbols, lines, and top x-axis follow the same notation from those of Fig. 15.

This article is copyrighted as indicated in the article. Reuse of AIP content is subject to the terms at: http://scitation.aip.org/termsconditions. Downloaded to IP: 168.96.66.153 On: Tue, 30 Jun 2015 17:10:17

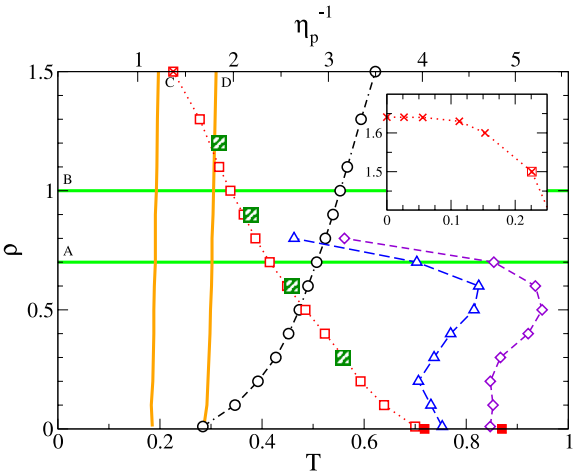

FIG. 17. Phase diagram for $N = 4$ with characteristic curves. Symbols, lines, and top x-axis follow the same notation from those of Fig. 15. The inset shows details of $\beta P_w = \rho$ at low temperatures.

the largest values of N, nearly coincides with the intersection of zero-energy and ideal gas pressure curves.[51]

We selected the $\beta P_w = \rho$ curve to verify the validity of the corresponding-states mapping between SW and AO models in confined systems. For this purpose, we used Metropolis-Rosembluth Monte Carlo calculations[52,53] to evaluate the density distribution of the AO system (for few values of ρ), and used contact theorem Eq. (10) to obtain βP_w. Thus, we seek for the value of η_p that produces $\beta P_w = \rho$. Extended corresponding states law [see Eq. (13)] was used to evaluate the temperature of the corresponding SW equivalent system. Figs. 15–19 show these results in green squares. The values of η_p^{-1} are given at the top horizontal x axis, while the equivalent temperature of the SW system can be read at the bottom axis. We found a general agreement between the Monte Carlo results for AO and EDMD simulation results for SW particles, within the analyzed range. At lower temperatures, near clusterization, the mapping between both systems becomes poorer. This is expected, because the use of the extended law of corresponding states is not documented for freezing temperatures.

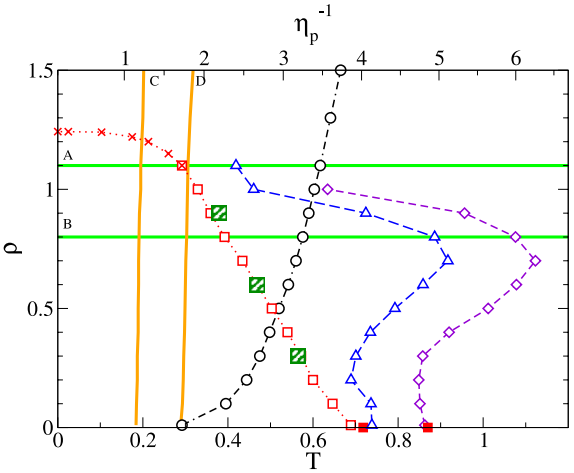

FIG. 18. Phase diagram for $N = 5$ with characteristic curves. Symbols, lines, and top x-axis follow the same notation as those of Fig. 15.

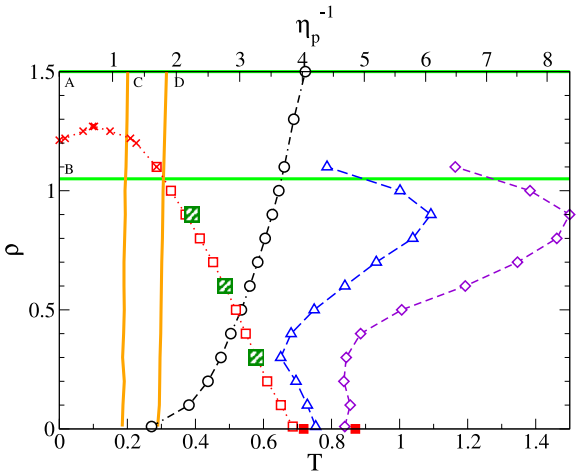

FIG. 19. Phase diagram for $N = 6$ with characteristic curves. Symbols, lines, and top x-axis follow the notation of Fig. 15.

Zero surface adsorption and surface tension curves indicate where there is no excess in surface of particle concentration or free energy, respectively. As it was mentioned in Sec. IV B, both are difficult to measure in the simulation. Γ and γ reveal a strong reduction of accuracy at very low density where the system is quasi-homogeneous and both quantities become very small. This makes specially hard to measure the value of T at which $\Gamma = 0$ and $\gamma = 0$ for $\rho \to 0$. In addition, given the fact that Γ and γ become ill defined at high densities, we do not evaluate zero surface excess in this case. In spite of the difficulties in measuring the curve $\Gamma = 0$, its behavior for $\rho \to 0$ is close to the theoretical value 0.8704, which is independent of N. In summary, the results presented here give a general idea of the position and shape of both curves in the (T, ρ) plane. Adsorption illustrates the relation between the density of particles at the center of the cavity and those closer to the wall. Towards the left side, where $\Gamma < 0$, the particles are more likely to be at the center of the cavity. For $\Gamma > 0$, at the right side, particles favor positions close to the wall.

Similar systems of SW colloids but with different values of the range parameter λ are also interesting to study, but they are beyond the scope of the present work. We expect that the increment (decrement) of λ will shift the temperature dependence in the phase diagrams to the left (right). For example, based on theoretical calculus,[30] for small values of $\Delta\lambda = \lambda - 0.1$, the $\beta P_w = \rho$ curve at $\rho \to 0$ evolves as $0.7186 + 4.255\,\Delta\lambda$ and $\Gamma = 0$ curve evolves as $0.8704 + 5.936\,\Delta\lambda$.

V. SUMMARY AND CONCLUDING REMARKS

In this work we studied thoroughly the properties of few colloidal particles confined in a spherical cavity. We adopt the short-range square well model and provide a deep characterization of the structural and thermal properties of systems of 2–6 particles in a spherical pore for the complete relevant ranges of density and temperature. Additionally, we compare the simulations with exact results for the case $N = 2$. Applying an extension of the corresponding states law to confined systems, we establish a mapping between the

This article is copyrighted as indicated in the article. Reuse of AIP content is subject to the terms at: http://scitation.aip.org/termsconditions. Downloaded to IP: 168.96.66.153 On: Tue, 30 Jun 2015 17:10:17

simulated square well system and the AO model, for effective interactions between colloids in a polymer-colloid mixture. We also developed the statistical mechanical approach to systems of few particles, SW and AO, in confinement and mapped the pressure on the wall at a given temperature in the SW system to the equivalent packing fraction of polymers in the AO system.

The structure of the system ranging from low density to almost caging of the particles in the cavity was characterized through the pair correlation function and density profiles for the entire relevant range of temperatures. We described the geometry of the clusters at low temperatures, dominated by energy minimization. For $N = 6$, we found two possible isoenergetic structures, identified from the shape of the pair-pair correlation function. One of them, with fewer symmetries, is more likely, due to a higher entropy, given by the larger number of possible states.

Thermal bulk properties such as energy and pressure on the wall were calculated and characterized. Different effects of confinement were also studied, identifying their energetic or entropic origin and focusing on the inhomogeneities present in the system. Surface properties were analyzed with quantities reminiscent of surface tension and adsorption of macroscopic square well system. We do not intend to make any claim about the validity of surface tension or adsorption for these nano-systems, but their careful measurement for few-particle systems can serve as a starting point to analyse up to which extent these quantities can be used far from the thermodynamic limit, or identify new physical observables to describe interface properties in the nano-scale.

We characterized the morphology of these systems, defining different regions of similar behavior and criteria to provide phase diagrams on the (T, ρ) plane, for the different number of particles. In this phase diagram, we identified temperature regions where the system behaves as a rigid cluster, as a plastic cluster, and a region where the system dissociates, up to the limit of hard sphere behavior at very high temperatures. In the density domain, we recognized regions with different degrees of inhomogeneity which can be classified in the following categories: low-to-moderate, moderate to excluded volume, and excluded-volume to caging regions. We defined several characteristic curves in the phase diagram, such as that of zero energy, ideal gas pressure, zero adsorption, and zero surface tension. These lines are meaningful marks in the phase diagram, that were used as a complement for the analysis.

This comprehensive characterization of the mass distribution of a few particles in a spherical pore, the arrangement of the particle clusters at low temperatures, and phase diagrams, which delimit distinctive behaviors in the density-temperature plane is hopefully useful to understand the properties of hollow-nanoparticles confining colloids or molecules. In the studied case, the wall is neutral and, therefore, some shift in the phase diagrams should be expected for experimental systems with attractive walls. However, the inclusion of a short-range attraction among particles and excluded-volume repulsion may be representative of a wide number of systems in the area of nano-rattles, yolk-shell particles, and other developments of highly confined colloids.

ACKNOWLEDGMENTS

Financial support through Grant Nos. PICT-2011-1887, PICT-2011-1217, PIP 112-200801-00403, INN-CNEA 2011, and PICT-E 2014 is gratefully acknowledged.

APPENDIX: EFFECTIVE POTENTIAL AND AO PARTITION FUNCTION

We show here how to transform Eq. (6) into Eq. (7). To this end, we analyze the term $\sum_{N_p} \frac{z_p^{N_p}}{N_p!} Z_{N,N_p}$ in Eq. (6), where the (canonical ensemble) colloid-polymer mixture CI reads

$$Z_{N,N_p} = \int_{V^N} \int_{V_p^{N_p}} e^{-\beta(\phi_{cc}+\phi_{cp})} d\mathbf{r}_p^{N_p} d\mathbf{r}_c^N, \qquad \text{(A1)}$$

with $\phi_{cc} = \sum_{i,j} \phi_{ij}^{(cc)}$, $\phi_{cp} = \sum_i^{(c)} \sum_k^{(p)} \phi_{ik}^{(cp)}$. $\phi_{ij}^{(cc)}$, and $\phi_{ik}^{(cp)}$ are the spherically symmetric pair potentials. Note that the region $\mathcal{C}$ where the center of colloids is confined (with volume V) is different to the region $\mathcal{P}$ where the center of polymers lies (with volume V_p). In fact, the boundary of $\mathcal{P}$ must be placed in a region where the polymers reach their bulk properties. For the AO system with $q < 0.1547$ confined in a spherical pore, the smallest region $\mathcal{P}$ is a sphere with radius $R_0 + \sigma_p/2$.

Polymers behave as ideal gas particles. If we fix the position of the colloids, they exert a fixed external potential to the polymers and thus

$$\int_{V_p^{N_p}} e^{-\beta\phi_{cp}} d\mathbf{r}_p^{N_p} = \left(\int_{V_p} e^{-\beta\phi_{cp}} d\mathbf{r}_p \right)^{N_p} = Z_\otimes^{N_p}, \qquad \text{(A2)}$$

where $Z_\otimes$ is the CI of one polymer in V_p at fixed colloids. Furthermore,

$$\sum_{N_p} \frac{z_p^{N_p}}{N_p!} Z_{N,N_p} = \int_{V^N} e^{-\beta\phi_{cc}} \sum_{N_p} \frac{z_p^{N_p}}{N_p!} Z_\otimes^{N_p} d\mathbf{r}_c^N, \qquad \text{(A3)}$$

$$= \int_{V^N} e^{\left(-\beta\phi_{cc} + z_p Z_\otimes\right)} d\mathbf{r}_c^N, \qquad \text{(A4)}$$

and thus we can simply analyze the case of one polymer. We introduce the Mayer function for the colloid/polymer Boltzmann statistical weight $e_i = \exp\left(-\beta\phi_{i1}^{(cp)}\right) = 1 + f_i$ in $Z_\otimes$ to obtain

$$Z_\otimes = \int_{V_p} \left(1 + \sum_i f_i + \sum_{<ij>} f_i f_j + \cdots\right) d\mathbf{r}_p, \qquad \text{(A5)}$$

where higher order terms are products of three or more functions f concerning the position of three or more colloids. In this integrand, f_i is minus one for $\mathbf{r}_p$ such that the (center-to-center) i th-colloid to polymer distance fulfills $x_i < \sigma + \sigma_p$ and otherwise is zero. $f_i f_j$ is one if $\mathbf{r}_p$ fulfills both $x_i < \sigma + \sigma_p$ and $x_j < \sigma + \sigma_p$ and is zero otherwise, and so on. Once integrated, $Z_\otimes$ takes the form

$$V_p - \frac{4\pi}{3}\sigma^3(1+q)^3 N + \sum_{<ij>} V_o(r_{ij}) + \cdots. \qquad \text{(A6)}$$

Here, $V_o(r_{ij})$ is the overlap volume between two spheres with radius $(\sigma + \sigma_p)/2$ and extra terms include the overlap of at least three spheres. Turning to the integrand of Eq. (A4), we utilize the identities $z_p = \rho_p$ and $z_p V_p = N_p$ to obtain

This article is copyrighted as indicated in the article. Reuse of AIP content is subject to the terms at: http://scitation.aip.org/termsconditions. Downloaded to IP: 168.96.66.153 On: Tue, 30 Jun 2015 17:10:17

$$\exp\left(N_p - N_p^x\right)\exp\left[-\beta\sum_{<ij>}\phi_{\mathrm{HS}}(r_{ij}) + \rho_p\sum_{<ij>}V_o(r_{ij})\right], \tag{A7}$$

with $N_p^x = \rho_p v_{\mathrm{exc}} N$ and $v_{\mathrm{exc}} = \frac{4\pi}{3}\sigma^3(1+q)^3$. In addition, we neglected higher order terms in Eq. (A7). These terms are null if $q < 0.1547$. For $q \gtrsim 0.1547$, including the case $q = 0.2$ analyzed in the present work, one expects that three-body contribution will be negligible in comparison with two-body terms. Naturally, $\Xi_{p,h} = \exp N_p$ and $\beta\phi_{\mathrm{AO}}(r) = \beta\phi_{\mathrm{HS}}(r) - \rho_p V_o(r)$, where $\beta\phi_{\mathrm{AO}}(r)$ is the same expression given in Eq. (8). Therefore, Eq. (A4) is $Z_N^{(\mathrm{AO})}$. This demonstrates the equivalence between Eqs. (6) and (7).

The described procedure can be generalized in several ways. It is not restricted to the spherical pore, and thus, it applies to other pore geometries like cylinders, cuboids, slits, and single walls. Further extensions include the case of non-free polymers where both, colloids and polymers, are confined, the AO model with $q \gtrsim 0.1547$, and also other non-AO systems with more general interaction potentials. It can also be readily applied to systems of AO particles in spaces with dimensions other than three (discs and hyper-spheres), with $V_o(r)$ taken from Ref. 54.

[1]R. Ghosh Chaudhuri and S. Paria, Chem. Rev. **112**, 2373 (2012), pMID: 22204603.
[2]T.-T. Wang, F. Chai, C.-G. Wang, L. Li, H.-Y. Liu, L.-Y. Zhang, Z.-M. Su, and Y. Liao, J. Colloid Interface Sci. **358**, 109 (2011).
[3]J. Liu, S. Z. Qiao, S. Budi Hartono, and G. K. Lu, Angew. Chem. **122**, 5101 (2010).
[4]X. W. D. Lou, L. A. Archer, and Z. Yang, Adv. Mater. **20**, 3987 (2008).
[5]L. Tan, D. Chen, H. Liu, and F. Tang, Adv. Mater. **22**, 4885 (2010).
[6]S. Kalele, S. W. Gosavi, J. Urban, and S. Kulkarni, Curr. Sci. **91**(8), 1038 (2006).
[7]K. Landfester, Adv. Mater. **13**, 765 (2001).
[8]C. P. Royall, W. C. K. Poon, and E. R. Weeks, Soft Matter **9**, 17 (2013).
[9]C. P. Royall, A. A. Louis, and H. Tanaka, J. Chem. Phys. **127**, 044507 (2007).
[10]I. Urrutia and C. Pastorino, J. Chem. Phys. **141**, 124905 (2014).
[11]I. Urrutia and G. Castelletti, J. Chem. Phys. **136**, 224509 (2012).
[12]I. Urrutia, J. Chem. Phys. **135**, 024511 (2011); Erratum, *ibid.* **135**(9), 099903 (2011).
[13]I. Urrutia, J. Stat. Phys. **131**, 597 (2008), e-print arXiv:cond-mat/0609608.
[14]L. Acedo and A. Santos, J. Chem. Phys. **115**, 2805 (2001).
[15]L. Li, F. Sun, Z. Chen, L. Wang, and J. Cai, J. Chem. Phys. **141**, 054905 (2014).
[16]S. Rivera-Torres, F. del Río, R. Espíndola-Heredia, J. Kolafa, and A. Malijevský, J. Mol. Liq. **185**, 44 (2013).
[17]R. Espíndola-Heredia, F. d. del Río, and A. Malijevský, J. Chem. Phys. **130**, 024509 (2009).
[18]H. L. Vortler, K. Schafer, and W. R. Smith, J. Phys. Chem. B **112**, 4656 (2008).
[19]R. López-Rendón, Y. Reyes, and P. Orea, J. Chem. Phys. **125**, 084508 (2006).
[20]S. B. Kiselev, J. F. Ely, and J. R. Elliott, Mol. Phys. **104**, 2545 (2006).
[21]H. Liu, S. Garde, and S. Kumar, J. Chem. Phys. **123**, 174505 (2005).
[22]M. Khanpour, Phys. Rev. E **83**, 021203 (2011).
[23]T. F. Hartskeerl, Master thesis, Utrecht University, Faculty of Science, 2011.
[24]H. Neitsch and S. H. L. Klapp, J. Chem. Phys. **138**, 064904 (2013).
[25]J. C. Armas-Pérez, J. Quintana-H, and G. A. Chapela, J. Chem. Phys. **138**, 044508 (2013).
[26]H. C. Huang, W. W. Chen, J. K. Singh, and S. K. Kwak, J. Chem. Phys. **132**, 224504 (2010).
[27]S. Jana, J. K. Singh, and S. K. Kwak, J. Chem. Phys. **130**, 214707 (2009).
[28]X. Zhang and W. Wang, Phys. Rev. E **74**, 062601 (2006).
[29]D. L. Pagan and J. D. Gunton, J. Chem. Phys. **122**, 184515 (2005).
[30]I. Urrutia and G. Castelletti, J. Chem. Phys. **134**, 064508 (2011).
[31]Y. Reyes, Fluid Phase Equilib. **336**, 28 (2012).
[32]Y. Duda, J. Chem. Phys. **130**, 116101 (2009).
[33]K. Binder, P. Virnau, and A. Statt, J. Chem. Phys. **141**, 140901 (2014).
[34]A. Winkler, A. Statt, P. Virnau, and K. Binder, Phys. Rev. E **87**, 032307 (2013).
[35]A. Statt, A. Winkler, P. Virnau, and K. Binder, J. Phys.: Condens. Matter **24**, 464122 (2012).
[36]P. Germain and S. Amokrane, Phys. Rev. E **76**, 031401 (2007).
[37]M. López de Haro, C. F. Tejero, A. Santos, S. B. Yuste, G. Fiumara, and F. Saija, J. Chem. Phys. **142**, 014902 (2015).
[38]M. G. Noro and D. Frenkel, J. Chem. Phys. **113**, 2941 (2000).
[39]N. E. Valadez-Pérez, A. L. Benavides, E. Schöll-Paschinger, and R. Castañeda Priego, J. Chem. Phys. **137**, 084905 (2012).
[40]J.-P. Hansen and I. R. McDonald, *Theory of Simple Liquids*, 3rd ed. (Academic Press, Amsterdam, 2006).
[41]E. M. Blokhuis and J. Kuipers, J. Chem. Phys. **126**, 054702 (2007).
[42]S. L. Taylor, R. Evans, and C. P. Royall, J. Phys.: Condens. Matter **24**, 464128 (2012).
[43]P. Germain and S. Amokrane, Phys. Rev. E **81**, 011407 (2010).
[44]N. Gnan, E. Zaccarelli, and F. Sciortino, J. Chem. Phys. **137**, 084903 (2012).
[45]H. Hansen-Goos, M. A. Miller, and J. S. Wettlaufer, Phys. Rev. Lett. **108**, 047801 (2012).
[46]P. Charbonneau and D. Frenkel, J. Chem. Phys. **126**, 196101 (2007).
[47]M. P. Allen and D. J. Tildesley, *Computer Simulations of Liquids* (Clarendom Press, Oxford, 1987).
[48]B. J. Alder and T. E. Wainwright, J. Chem. Phys. **31**, 459 (1959).
[49]R. Tehver, F. Toigo, J. Koplik, and J. R. Banavar, Phys. Rev. E **57**, 17 (1998).
[50]J. Israelachvili, *Intermolecular and Surface Forces* (Academic Press, Burlington, MA, 2011).
[51]These curves were extrapolated from surface tension data in Ref. 19.
[52]N. Metropolis, A. W. Rosenbluth, M. N. Rosenbluth, A. H. Teller, and E. Teller, J. Chem. Phys. **21**, 1087 (1953).
[53]M. N. Rosenbluth and A. W. Rosenbluth, J. Chem. Phys. **22**, 881 (1954).
[54]I. Urrutia and L. Szybisz, J. Math. Phys. **51**, 033303 (2010).

This article is copyrighted as indicated in the article. Reuse of AIP content is subject to the terms at: http://scitation.aip.org/termsconditions. Downloaded to IP: 168.96.66.153 On: Tue, 30 Jun 2015 17:10:17